The Energy Driven Hot Carrier Model

Stewart E. Rauch and Fernando Guarin

Abstract The so-called "Energy Driven Model" for hot carrier effects in MOS devices was first proposed in 2005 as a replacement for the ubiquitous Lucky Electron Model (LEM) in the short channel regime (especially at or below the 130 nm node) [1]. As MOSFET size and voltage are scaled down, the carrier energy distribution becomes increasingly dependent only on the applied bias, because of quasi-ballistic transport over the high field region. The energy driven model represents a new paradigm of MOSFET hot carrier behavior in which the fundamental driving force is available energy, rather than peak lateral electric field as it is in the LEM. The model predictions are shown to be consistent with experimental impact ionization results. Experimental hot carrier degradation results for a wide range of technologies support the concept of a nearly universal carrier energy dependent cross section of hot carrier damage (S_{it}).

1 Introduction

Carriers (electrons or holes) can gain large kinetic energies from transit through regions of high electric field in the drain region of a CMOS device. When the mean carrier energy is significantly larger than that associated with the lattice in thermal equilibrium, they are called "hot," because historically the carrier kinetic energy was assumed to be approximately distributed with a thermal-like distribution ("Maxwellian") at an effective temperature higher than that of the lattice. This distribution is in a steady state with the local electric field, and its effective temperature is dependent on this field. If carriers gain enough energy to be injected into the gate oxide, or cause interfacial damage, they will introduce instabilities in the electrical characteristics of a MOSFET device. The damage rate is thus dependent on the lateral electric field. This is the basis of the popular "Lucky

S.E. Rauch (✉)
State University of New York at New Paltz, New Paltz, NY, USA
e-mail: s.rauch@ieee.org; stewrauch@gmail.com

F. Guarin
IBM Microelectronics, Hopewell Jct., NY, USA
e-mail: ferguarin@gmail.com

T. Grasser (ed.), *Hot Carrier Degradation in Semiconductor Devices*,
DOI 10.1007/978-3-319-08994-2_2

Electron Model" [2]. However, a new picture has emerged, known as the "Energy-Driven Model" [1, 3]. The assumption of a Maxwellian-like energy distribution in steady state with the local electric field increasingly breaks down as the size of the high field region is scaled below 100 nm or so (roughly 0.25 μm or less channel length technology), and technology power supply voltages scale down. As we shall see, quasi-ballistic transport in the high field region of MOSFETs at modern dimensions generally induces a rather shallow carrier energy distribution function up to the total energy available in the high field region, but then a sharp inflection downward at that energy, and a steep tail at higher energies. This sharp downward inflection or "knee" leads to a hot carrier damage rate that is dependent on the total available energy. In this sense, the energy driven model can be viewed as a sort of "compact model" for hot carrier degradation effects in current CMOS technologies.

2 The Lucky Electron Model

The Lucky Electron Model (LEM) of C.M. Hu et al. [2] remains firmly entrenched as the guiding principle of most industry standard hot carrier models and projection methodologies. The fundamental concept as applied to silicon can be traced back to Shockley [4], and originally to Townsend's theory of *gas discharge* developed in the early 1900s [5]. In a gas discharge, free electrons are accelerated by the electric field until such time as they collide with a gas atom. The interaction may ionize the atom, leading to two free electrons, which in turn will be accelerated by the field. The process leads to "avalanche breakdown" of the gas. This is why the phrase "impact ionization" is used. The probability of an electron's traveling a distance at least d before suffering a collision is,

$$P(d) = e^{-d/\lambda}, \tag{1}$$

where λ is called the "mean free path." The electron is assumed to lose all of its kinetic energy in the collision. Since the energy, E, gained by the electron from the electric field, F, is E = qdF, the electron energy distribution is given by

$$f(E) = P(E) = e^{-E/q\lambda F}. \tag{2}$$

This is the basis of the Lucky Electron Model. This distribution has a very similar energy dependence to a thermal, or "Maxwellian" energy distribution (per degree of freedom) with an effective temperature, T_{EFF}, of

$$T_{EFF} = \frac{q\lambda F}{k}. \tag{3}$$

This coincidental resemblance to an energy distribution in thermal equilibrium is the historical reason for the designations "hot electron" and "hot carrier."

Note: The electrons do not actually behave in a thermal way—a thermal velocity distribution would be isotropic, and the Lucky Electron Model actually posits purely ballistic behavior—velocity is strictly along the field direction.

Next, to model either the impact ionization rate, or the hot carrier damage rate, another simplifying assumption is made that both of these exhibit very sharp energy thresholds. That is, the rates are zero for electron energy below the threshold, and essentially constant above.

It is recognized that the electric field is not spatially constant, so the quantity F is replaced by F_m, the maximum field, since this is where the rates should peak. Under these assumptions, the ratio of substrate current, I_{sub}, to drain current (approximately the impact ionization ratio), is given by,

$$\frac{I_{sub}}{I_D} = A\mathrm{e}^{-\phi_i/\mathrm{q}\lambda F_m}, \tag{4}$$

where ϕ_i is the threshold energy for impact ionization. And the hot carrier rate, defined as the inverse of the hot carrier lifetime, τ, divided by drain current, is then,

$$\frac{1}{\tau I_D} = B\mathrm{e}^{-\phi_{it}/\mathrm{q}\lambda F_m}, \tag{5}$$

and ϕ_{it} is the threshold energy for hot carrier damage.

Two forms of hot carrier acceleration factor can be derived from Eqs. (4) and (5). The first is the relation between τ and I_{sub}:

$$\frac{1}{\tau I_D} = C\left(\frac{I_{sub}}{I_D}\right)^{\phi_{it}/\phi_i}, \tag{6}$$

By comparison with photon induced emission rates, the values of ϕ_{it} and ϕ_i were "inferred" to be about 3.7 and 1.3 eV, respectively, thus the ratio ~2.9. It has become very popular to use this equation to extrapolate experimental hot carrier data taken at high substrate currents under stress voltages down to a maximum use supply voltage $V_{DD,MAX}$ (using the measured substrate current at $V_{DS} = V_{DD,MAX}$). Since the peak lateral electric field is proportional to the drain bias to channel pinch-off drop $V_{DS} - V_{DSAT}$, where V_{DSAT} is the potential at the "pinch-off" or "saturation" point in the channel, the following equation is often used for the impact ionization rate:

$$\frac{I_{sub}}{I_D} = A\exp-\left[\frac{b}{(V_{DS}-V_{DSAT})}\right], \text{ or} \tag{7a}$$

$$\frac{I_{sub}}{I_D} = A\,(V_{DS}-V_{DSAT})\exp-\left[\frac{b}{(V_{DS}-V_{DSAT})}\right] \tag{7b}$$

A second cruder form of hot carrier voltage acceleration is loosely related:

$$\tau \approx De^{-V_0/V_{DS}}, \tag{8}$$

which is also highly used for lifetime extrapolation.

3 Realistic Carrier Energy Distribution Functions

3.1 Uniform Electric Fields

Even for the case of a uniform electric field of relatively large extent, Shockley's Lucky Electron Model (and Hu's extension), is, of course, an extreme simplification of the actual physical processes involved, and has been criticized by many authors [6–11]. The major flaw seems to be the analogy with gas discharge—an "impact" or scattering event will cause the carrier to lose all of its kinetic energy. Since phonon interaction is the dominant physical carrier scattering mechanism, momentum transfer can be large, but the carrier energy loss (or gain) per collision is limited by the optical phonon energy (∼63 meV in silicon). Thus, the high field transport is more a matter of "lucky drift" [7] or "lucky scattering" [9]. Carrier EDF's in silicon under these conditions have been simulated using various techniques. The general characteristic of the simulated EDF's is downward curvature. That is, rather than an approximately constant slope of ln(f) versus energy (as a Maxwellian has), these slopes are decreasing (more negative). However, Goldsman et al. [12] points out that the lucky electron model can still produce reasonably accurate predictions under these conditions if an energy dependent mean free path is used (between about 50 and 80 Å).

3.2 Non-uniform Electric Fields, Short Extents, and Limited Potential Drops

The lateral electric field in MOSFETs past the saturation point in the channel is highly non-uniform [13], being approximately an exponential function of lateral distance [14]:

$$F \propto e^{y/l} \tag{9}$$

l is a scale factor that is generally on the order of 10 % of "L_{nom}" (the minimum design channel length for a given MOSFET device design). The length of the high field region (after the pinch-off or saturation point in the channel) is some multiple of l, but even for a quarter micron device, is probably less than or about equal

to 100 nm, which is a short enough extent to influence the EDF. In addition, the maximum energy that is available from the field is becoming increasingly limited by scaling down of the power supply voltage. Many authors have shown that the EDF under these conditions has a significant knee near the maximum energy available from this steep potential drop at the drain [15–23]. This is approximately the potential from the drain to the channel "pinch-off" point [17] (which will be called 'V_{EFF}' here). Above this knee, there is a "thermal" tail which is due to carriers which have gained nearly the maximum possible from the electric field, and also absorbed a net positive thermal energy from phonon collisions. As CMOS device dimensions are made smaller and the supply voltage decreases, there are two main effects to the EDF. First, the EDF becomes shallower for $E < qV_{EFF}$. Second, the knee near $E = qV_{EFF}$ strengthens, and moves down into the energy range of importance. The general characteristics of these EDF's (at about the $L_{nom} = 100$ nm technology node) are shown in Fig. 1 for two values of V_{EFF} (cf. [17]). If the position is within the neutral drain region, then there will be a contribution from the cold drain carriers, which can be seen here below 0.2 eV. These can be ignored (since they will not contribute to hot carrier effects), and the EDF can be fit to an idealized distribution that is 'LEM-like' for $E < qV_{EFF}$, but is truncated by a thermal tail for higher energies:

$$\begin{aligned} f_I(E) &\propto \exp\left(-\chi E/qV_{EFF}\right), \quad E \le qV_{EFF} \\ &\propto e^{-\chi} \exp\left[\left(qV_{EFF} - E\right)/nkT\right], \quad E > qV_{EFF} \end{aligned} \tag{10}$$

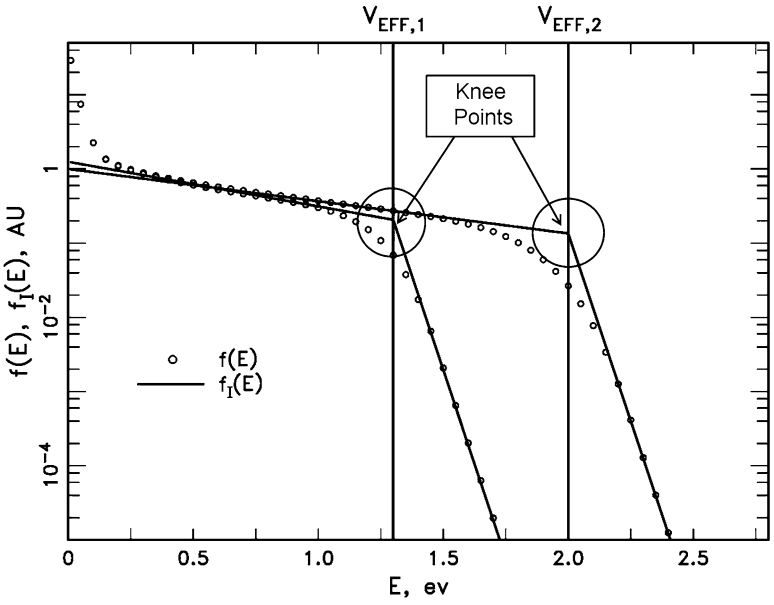

Fig. 1 Generalized quasi-ballistic EDF typical of the literature [17], f(E), and idealized EDF, $f_I(E)$, for two values of V_{EFF} ($\chi \sim 2$)

Use of this EDF will simplify later discussions. Typical values of χ derived from the literature are dependent on L_{nom}: $\chi \sim 0$ for 25 nm, 1 for 50 nm, 2 for 100 nm, and 4 for 250 nm. The weak V_{EFF} dependence of χ, and the normalization factor for f are neglected.

4 The Energy Driven Model

4.1 Introduction

The starting point for the energy driven model is a simplified expression for hot carrier rates due to an energy mediated process such as impact ionization or interface state generation. The rates are approximately determined by an integral of the following form:

$$Rate = \int f(E)S(E)dE, \tag{11}$$

where f is the energy distribution function (EDF), and S = interaction cross section or scattering rate. The density of states is not explicitly included here, and can be considered to be part of f(E), or else neglected. As we shall see, the integrand of this rate equation will generally peak at one or more points, which are referred to as 'dominant energies' because carriers near these energies dominate the respective hot carrier rate.

This occurs when,

$$\frac{d\ln f}{dE} = -\frac{d\ln S}{dE}. \tag{12}$$

Mathematically, the dominant energy can be controlled by 'knee' points (points of high curvature) of either ln(f) or ln(S). Both the lucky electron and energy driven models are limiting assumptions to allow a simple unified equation of hot carrier induced damage effects. While the lucky electron model implicitly assumes that the knee points of the ln(S) functions drive the dominant energies, the energy driven model is based on the idea that the knee points of ln(f) drive the dominant energies [1].

The LEM represents the large (long high field region) device, and high voltage limit. However, we know that as the power supply voltage is scaled down, the EDF becomes increasingly limited at energies of importance to hot carrier effects (generally less than 5 eV or so). In the LEM, the EDF has no significant knee and the dominant energies for impact ionization (II) and interface state generation (ISG) are determined by knee points in the respective cross sections (thought to be very close to energy thresholds ϕ_i and ϕ_{it} in the LEM.) Figure 2 is a conceptual schematic of this concept for impact ionization. In keeping with the thinking of the time, the Keldysh model ($\propto(E - E_G)^2$) [24] is used for S_{ii}.

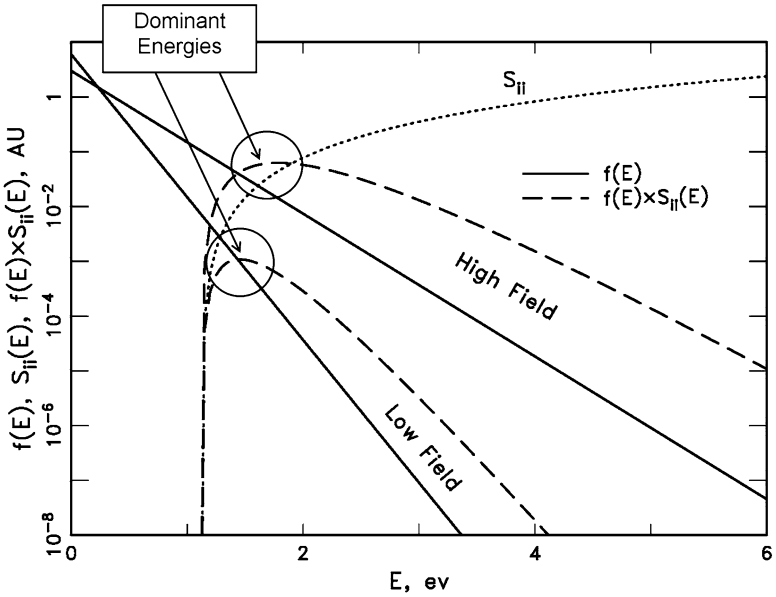

Fig. 2 A graphical representation of the field driven hot carrier paradigm applied to impact ionization

The II and ISG rates are then 'field driven': (1) The dominant energies are weak functions of bias conditions. (2) The hot carrier bias dependencies are due almost solely to the changes in the EDF slope with field.

4.2 Conditions for Energy Driven Hot Carrier Rates

To illustrate the conditions under which the hot carrier behavior is energy driven, we use the idealized EEDF, $f_I(E)$, which collapses the knee to a single point. Recall,

$$\begin{aligned} f_I &\propto \exp\left(-\chi E/qV_{EFF}\right), \quad E \le qV_{EFF} \\ &\propto e^{-\chi}\exp\left[\left(qV_{EFF}-E\right)/nkT\right], \quad E > qV_{EFF} \end{aligned} \tag{13}$$

A scattering rate of the following form is used: $S = A(E - E_{TH})^p$. In this idealized case, the energy driven regime can be defined as when the dominant energy $= qV_{EFF}$. Using Eq. (12), this can easily be shown to be,

$$E_{TH} + pnkT \le \quad qV_{EFF} \quad \le \frac{E_{TH}}{1-p/\chi}, \qquad \chi > p \tag{14}$$

The field driven regime is when V_{EFF} is above this region. If $\chi < p$, there is no field driven regime. For V_{EFF} below this region, the dominant energy is in the thermal tail. This might be referred to as the 'thermal tail driven' regime [14]. To give some approximate numbers as examples, let S = impact ionization rate for electrons (S_{ii}), $E_{TH} = E_G = 1.12$ eV, $p \sim 4.6$ for electron induced impact ionization [25], and using n = 1.66 [26], T = 300 K,

$$1.317\ eV \leq \quad qV_{EFF} \quad \leq \frac{1.12\ eV}{1 - 4.6/\chi}, \qquad \chi > 4.6 \tag{15}$$

Since the typical values of $\chi < 4.6$ for $L_{nom} < 0.25$ mm, for any NFET device of a quarter micron or smaller technology, the impact ionization will be energy or thermal tail driven for any V_{EFF}. The case for ISG remains to be seen, because S_{IT} is a priori unknown. This is illustrated in Fig. 3 for this example, $\chi = 3$, and $V_{EFF} = 1.5$ and 2 V. In this figure the S_{II} used is the more modern model of Kamakura et al. ($\propto (E - E_G)^{4.6}$) [25], which is 'softer' (less curvature near threshold) than the older II models. The dominant energy is equal to V_{EFF} for these values.

Figure 4 shows the thermal tail driven situation for $V_{EFF} = 1.2$ V. Now the dominant energy is no longer equal to qV_{EFF}, but moves into the thermal tail.

If the knee determines the dominant energies, then the II and ISG rates are "energy driven": (1) The dominant energies track with bias condition. (2) The

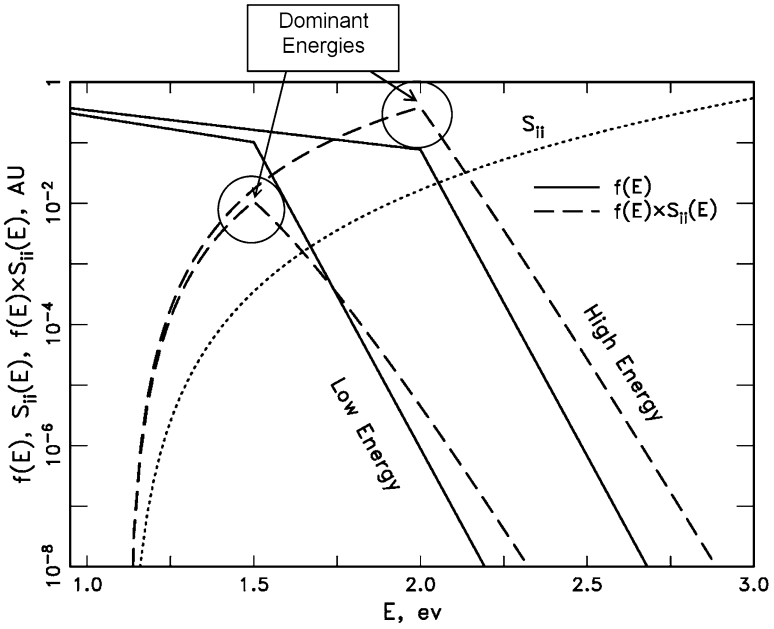

Fig. 3 A graphical representation of the energy driven hot carrier paradigm applied to II ($V_{EFF} = 1.5$ and 2 V)

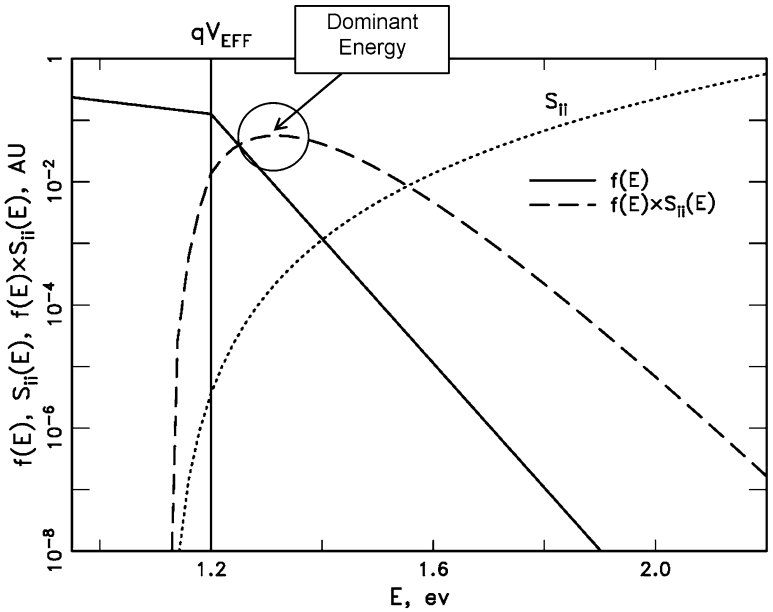

Fig. 4 A graphical representation of the thermal tail driven regime ($V_{EFF} = 1.2$ V)

hot carrier bias dependencies are due primarily to the energy dependence of the S functions, through the bias dependencies of V_{EFF}. The field dependence of the carrier EDF (value of χ) is secondary.

In the energy driven regime, the impact ionization rate is approximately proportional to the scattering rate,

$$r_{ii} \equiv \frac{I_{sub}}{I_D} = \int f_I(E) S_{ii}(E) dE \approx A_{ii} e^{-\chi} S_{ii}\,(qV_{EFF}) \tag{16}$$

The integral $r_{ii}(V_{EFF})$ is compared against $S_{ii}(qV_{EFF})$ in Fig. 5. It can be seen that r_{ii} closely follows S_{ii} down to the critical V_{EFF} value. Below this, r_{ii} follows a thermal slope approximately equal to nT.

5 Experimental Impact Ionization Measurements

We use experimental impact ionization results on two device types from the IBM hot carrier DC stress database to demonstrate the energy driven impact ionization concept. (Many more device types will be used later.) Characteristics of these two device types are summarized in Table 1. The database includes a range of channel lengths, as well as a large number of stress conditions, varying both V_{GS} and V_{DS}.

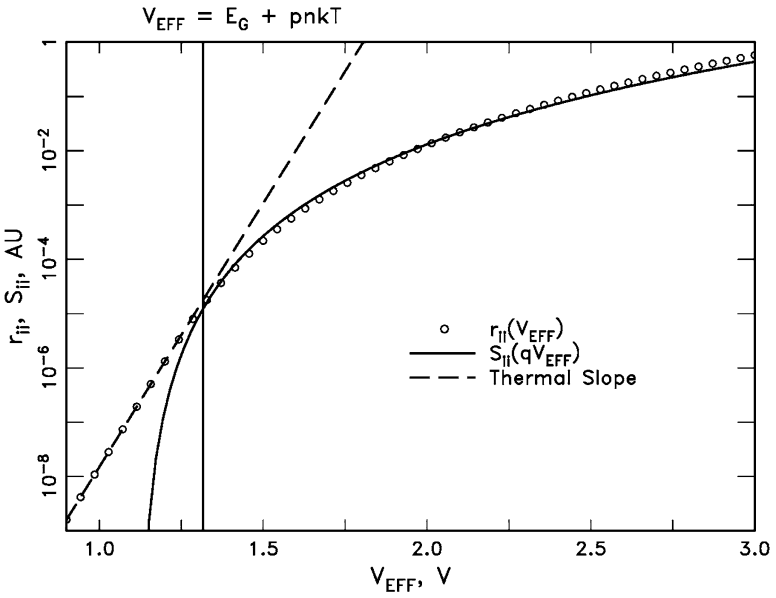

Fig. 5 Comparison of r_{ii} integral with S_{ii}

Table 1 Device types for impact ionization

Device type	1	2
Technology	A	
Node	90 nm	
Tech. device option	SG	DG
V_{DD}, V	1.2	2.5
L_{nom}, nm	63	240
T_{ox}, nm	1.6	5.2
Gate Insulator	Nitrided SiO_2	SiO_2
Reference	[27]	

The calculation of V_{EFF} was performed in the following way:
V_{EFF} = effective potential drop from channel to drain:

$$V_{EFF} = V_0 + V_{DS} - V_{DSAT} \tag{17}$$

where V_0 = added potential due to halo [28, 29], and/or 'source function', (total expected to be on the order of several hundred mV), and V_{DSAT} = pinch-off or saturation voltage. An approximate equation for V_{DSAT} from Taur and Ning [30] is used,

$$V_{DSAT} = \frac{2\left(V_{GS} - V_T\right)/m}{1 + \sqrt{1 + \frac{2(V_{GS}-V_T)}{mF_C(L-L_s)}}}, \tag{18}$$

Table 2 V_{TSAT} parameters

Device type	F_C, mV/nm	m_0	l_m, nm	L_S, nm
1, NFET	2.5	0.25	6	25
2, NFET	2.5	0.25	35	100
1, PFET	8	0.21	11	20
2, PFET	9	0.44	11	80

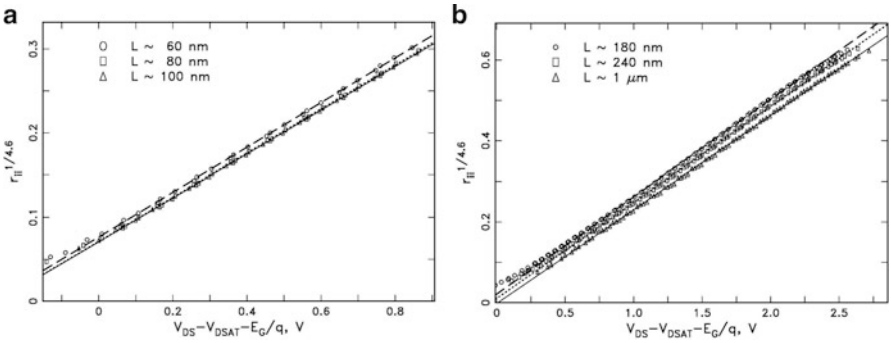

Fig. 6 *Points*: Measured NFET impact ionization ratio, $r_{ii}^{1/p}$, for three channel lengths versus calculated $V_{DS} - V_{DSAT} - E_G/q$. *Lines*: straight line fits. (**a**) Device Type 1, NFET; (**b**) Device Type 2, NFET

where F_C = critical field for velocity saturation, $L = L_{POLY}$ or L_{EFF}, L_S = length of velocity saturated region, and m = body effect coefficient. The V_T value used was the saturated V_T measured at time 0 (a weak function of V_{DS}). The value of m was determined by the sub-threshold slope in linear mode (no V_{DS} dependence was included). The channel length dependence was fit to a simple model:

$$m(L) = 1 + m_0 + \frac{l_m}{L - L_S} \tag{19}$$

L_S is also a weak function of V_{DS}; this was ignored, and was estimated by $0.4L_{nom}$ for NFETs, and $0.3L_{nom}$ for PFETs. The parameters are listed in Table 2.

The measured body currents are corrected for gate and drain leakage currents. The ambient temperature is 303 K for all measurements in this section. Lacking precise knowledge of V_0, the data are plotted as $y = r_{ii}^{1/p}$ vs. $x = V_{DS} - V_{DSAT} - E_G/q$ for a range of V_{DS} and a few V_{GS} points near and just above V_T. The generally accepted value of p = 4.6 was used for NFETs. This should yield a straight line with an x-intercept of $-V_0$. The fitted values will be different from "actual" values due to the deviation between the r_{ii} integral and S_{ii} shown in Fig. 5. Although it conceptually does have some physical basis, we will treat V_0 purely from an empirical standpoint. Figure 6 shows this plot for device types 1 and 2, NFET. The expectation of linearity is fairly well met, except for low values of x, as predicted by Fig. 5.

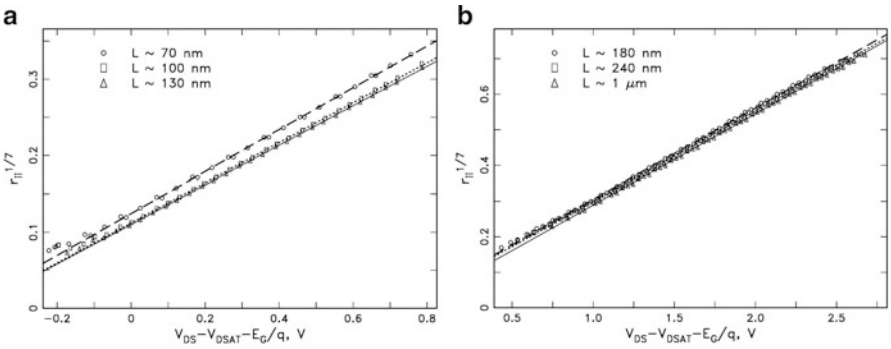

Fig. 7 *Points*: Measured PFET impact ionization ratio, $r_{ii}^{1/p}$, for three channel lengths versus calculated $V_{DS} - V_{DSAT} - E_G/q$. *Lines*: straight line fits. (**a**) Device Type 1, PFET; (**b**) Device Type 2, PFET

Table 3 Fit values for a and V_0

Device	L, nm	a, V^{-1}	V_0, V
1, NFET	60	0.27	0.29
	80	0.26	0.27
	100	0.26	0.27
2, NFET	180	0.24	0.09
	240	0.24	0.05
	1,000	0.23	0.00
1, PFET	70	0.27	0.45
	100	0.26	0.43
	130	0.26	0.43
2, PFET	180	0.26	0.19
	240	0.25	0.18
	1,000	0.26	0.13

For PFETs, $p = 7$ was chosen to produce reasonably straight lines. This does not agree with published values in the literature, which generally are much less, along with threshold energies greater that the bandgap ($E_{TH} > E_G$). For example, Kamakura [31] reports a values of $p = 3.4$, $E_{TH} = 1.49$ eV. The impact ionization in PFETs may have a more complicated energy (and momentum) dependence than our simple model.

The PFET data for device types 1 and 2 are shown in Fig. 7.

The slope (a) and x-intercept (V_0) values of the straight line fits for all these devices are listed in Table 3.

The measured NFET data follow the energy driven prediction, Eq. (16), almost exactly, for $\sim 1.4\ V < V_{EFF} < \sim 3.7$ V. Although the values for V_0 are empirical, the fact that the expected slope ($p = 4.6$) and energy threshold ($\sim E_G$) of the $S_{ii}(E)$ function can be reproduced so well, independently of device scaling, must be viewed as an experimental verification of the energy driven model. This also provides

justification for extending this approach to the experimental determination of the S_{it} function. Again, the experimentally determined PFET II parameters ($p \sim 7$, and $E_{TH} \sim E_G$) are not generally accepted in the literature, which is unclear for these parameters. Levels are remarkably constant between technologies-this implies that the parameter χ has little effect.

6 Short Range Carrier–Carrier Scattering Effects

Short range, or coulombic, carrier–carrier scattering is a mechanism whereby a carrier can gain even more energy than qV_{EFF}. There is a small probability that two high energy carriers undergo a scattering process so that one gains much of the total kinetic energy, leading to a small electron population of carriers up to about twice qV_{EFF}. Several authors [32–36], applying Monte Carlo or other simulation techniques to nMOSFETs, have predicted that at drain voltages below about 3 V, electrons "heated" by e–e scattering (EES) should dominate the high energy tail of the electron energy distribution function (EEDF). Thus, EES events have probably been playing an increasingly important role in the HC degradation of nMOSFETs as the supply voltage is scaled down. Carrier–carrier scattering (CCS) induces a second, weaker knee at just less than $2qV_{EFF}$, (and an even weaker knee at somewhat below $3V_{EFF}$, etc., which will be neglected here.) Adding c–c scattering effects to the base EDF and an idealized EDF are demonstrated in Fig. 8.

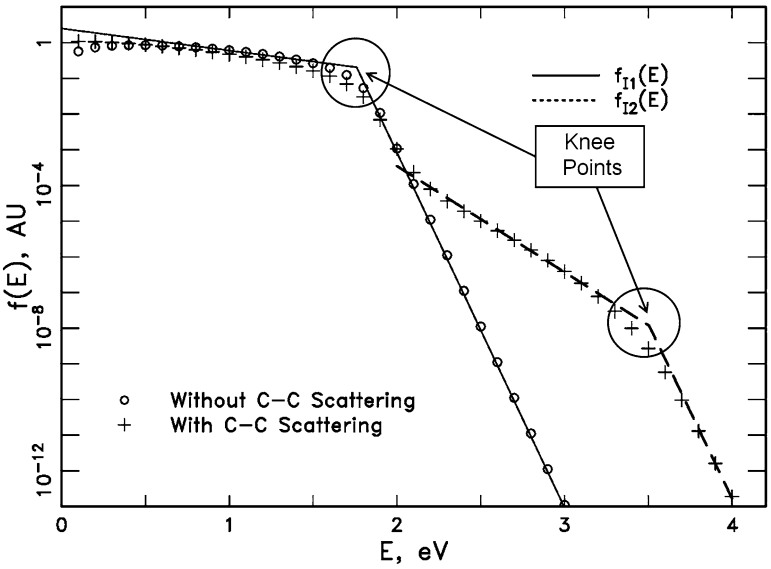

Fig. 8 EDF with and without C–C scattering tail and idealized EDF

The idealized EDF is:

$$f_I(E) = f_{I1}(E) + f_{I2}(E) \tag{20a}$$

$$\begin{aligned} f_{I1} &\propto \exp\left(-\chi_1 E/qV_{EFF}\right), \quad E \le qV_{EFF} \\ &\propto e^{-\chi_1} \exp\left[\left(qV_{EFF} - E\right)/nkT\right], \quad E > qV_{EFF} \end{aligned} \tag{20b}$$

$$\begin{aligned} f_{I2} &= 0, \quad E \le qV_{EFF} \\ &= a_{cc} {V_{EFF}}^{-3/2} \exp\left(-\chi_2 E/qV_{EFF}\right), \quad qV_{EFF} < E < 2qV_{EFF} \\ &= a_{cc}\, e^{-2\chi_2} {V_{EFF}}^{-3/2} \exp\left[\left(2qV_{EFF} - E\right)/nkT\right], \quad E > 2qV_{EFF} \end{aligned} \tag{20c}$$

The $V_{EFF}^{-3/2}$ term is due to the energy dependence of the c–c scattering cross section. Since the c–c scattering rate per carrier is approximately proportional to the carrier density in the energy range between V_{EFF} and $2V_{EFF}$, the relative level of f_{I2}, a_{cc}, has a linear I_D dependence. For this example, $V_{EFF} = 1.76$ V, $\chi_1 = 2.5$, $\chi_2 = 11.5$. The value of χ_2 depends on χ_1 and the energy dependence of the c–c scattering cross section. This approximate expression for χ_2 will be used here:

$$\chi_2 \approx 9 + \frac{\chi_1}{2} \tag{21}$$

The relative impact of the knee of the CCS tail to impact ionization can be bounded in the following way. Assuming a reasonable upper limit for the ratio of the tail population at its knee just below $2V_{EFF}$ to the base population at V_{EFF} of about 10^{-5}, the ratio of peak $f(E) \times S_{ii}(E)$ at the tail knee to that at the base knee is,

$$\text{ratio} < 10^{-5} \frac{S_{ii}\left(2qV_{EFF}\right)}{S_{ii}\left(qV_{EFF}\right)} = 10^{-5} \left(\frac{2qV_{EFF} - E_G}{qV_{EFF} - E_G}\right)^p \tag{22}$$

For electrons ($p = 4.6$), this ratio will exceed unity only for $V_{EFF} < 1.23$ V, which is inside the thermal tail driven regime. It appears that EES is too weak at reasonable carrier concentrations to contribute substantial impact ionization in the energy driven regime (at the tail knee), although lower energy parts of the EES tail will contribute at around bandgap or sub-bandgap V_{EFF} ($<1.3 - 1.4$ V) [36]. Even for holes ($p = 7$), unity ratio is at $V_{EFF} = 1.47$ V, just barely above the critical point for holes (1.42 V). This will appear as an CCS induced enhancement of the thermal tail contribution, and will not be modelled correctly by an energy driven approximation.

However, for NFETs, it is well established that the hot carrier damage rate is quadratic in I_D over much of the V_{GS} range (for a given energy) [3, 37, 38] implying that the knee of the EES tail does drive the rate. In this case, the hot carrier damage rate can be written as the energy driven approximation,

$$R_{ISG}\left(V_{EFF}\right) \approx A_1 I_D S_{it}\left(qV_{EFF}\right) + A_2 {I_D}^2 S_{it}\left(qm_{EE}V_{EFF}\right) \tag{23}$$

S_{it} is the interface state generation (ISG) scattering rate, and the parameter m_{EE} represents the ratio of the dominant energy (for ISG) due to the CCS tail to that due to the base distribution. Because of the relative weakness of the CCS knee, this may tend to be somewhat less than two. Simulations suggest values of $1.7 - 1.95$ (depending on technology) are reasonable. A_1 and A_2 are constants to be experimentally determined for each technology—any weak V_{EFF} dependencies are again ignored.

7 Experimental Hot Carrier Degradation Measurements

Hot carrier results on a cross section of the IBM hot carrier database consisting of seven device types (including the two already introduced) illustrate the energy driven hot carrier model to data comparison. Characteristics of these seven device types are summarized in Table 4. (Types 1 and 2 are repeated.)

Whereas the best measure of ISG from I–V characteristics would seem to be $\Delta(1/g_{mlin,max})$ [37, 43], the parameter $\Delta(1/I_{ON})$ (where $I_{ON} = I_D$ @ $V_{GS} = V_{DS} =$ technology power supply voltage V_{DD}) has proven to be much more robust over the entire range of stress conditions and channel lengths in the database. However, this damage metric displayed additional channel length (L) and threshold voltage (V_T) dependencies. These were normalized out by using this definition for R_{ISG} ("ISG rate"):

$$R_{ISG} \equiv \frac{1}{\text{Time to 5\% change of } \left\{ \Delta \left({I_{ON}}^{-1} \right) \left(\frac{L}{L_{nom}} \right)^{b} (V_{DD} - V_T) \right\}^{-1}} \tag{24}$$

$b \sim 1 - 1.5$. The V_T value used was the saturated V_T measured at time 0 (before stress).

All data in this section was taken at $T = 303$ K.

7.1 NFET Hot Carrier Data

The hot carrier data for NFETs generally show the three current regimes such as earlier reported by us [37, 38] and others [3]. These regimes are demonstrated in Fig. 9 for device type 4, NFET, as an example. The current dependence is observed when the energy dependence is approximately normalized out by dividing the ISG damage rate by $V_{EFF}{}^{p}$, ($p = 25$, determined empirically). I and II are the linear and quadratic regimes. III is the "high-V_G regime", or "high current regime". The physical reasons for an increasing damage rate in regime III are uncertain, but the effect has been attributed in the literature to various causes:

Table 4 Device types for hot carrier results

Device type	1	2	3	4	5	6	7
Technology	A			B	C	D	E
Node	90 nm			180 nm	90 nm	28 nm	14 nm
Dev. Opt.[a]	SG	DG	EG	–	SG	SG	SG
V_{DD}, V	1.2	2.5	1.5	1.8	1.0	1.0	0.8
L_{nom}, nm	63	240	100	120 (N)150 (P)	45	30	20
T_{ox}, nm	1.6	5.2	2.2	3.5	1.1	1.4[b]	1.2[b]
Gate Stack	Nitr. SiO_2, Poly	SiO_2, Poly	Nitr. SiO_2, Poly	Nitr. SiO_2, Poly	Nitr. SiO_2, Poly	HKMG	HKMG
Reference	[27]			[39]	[40]	[41]	[42]

[a]Many of these technologies have multiple device design options for various supply voltages (Dev. Opt.)
[b]Equivalent SiO_2 oxide thickness

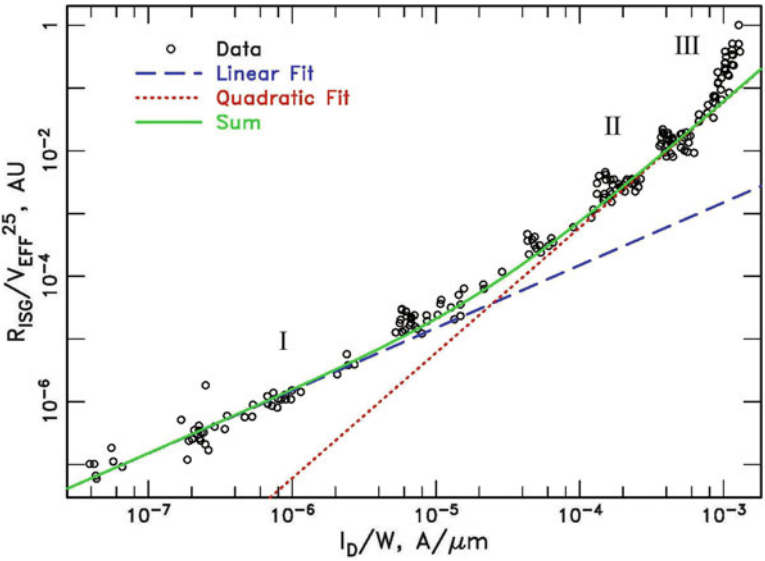

Fig. 9 Drain current dependence of hot carrier damage rate (Device Type 4, NFET)

1. Oxide field dependence of H bond breaking [43].
2. Increase of e–e scattering, and shift of potential minimum to SiO_2 interface [38].
3. Multi-vibrational excitation effects which become important at high I_D [3, 44]. For an in-depth discussion of multi-vibrational excitation, refer to chapter "The Spherical Harmonics Expansion Method for Assessing Hot Carrier Degradation" [45].
4. Localized self-heating in the drain region [46].

It is observed that the linear mechanism dominates only for low drain currents, typically $I_D < 10^{-4}$ to 10^{-5} A/um. This has several ramifications for this regime. The hot carrier damage rate is low, because of the low I_D. V_{GS} is close to, or below V_T, therefore V_{DSAT} is small, and V_{EFF} has little L dependence. Also, I_D is a strong function of V_{GS}. Because of these factors, there are many fewer stresses in our database in regime I than II, and the data in regime I tends to be "sparse" when plotted versus V_{EFF}. In fact, the linear regime results in relatively weak hot carrier degradation, and can usually be ignored for evaluating hot carrier shifts during typical CMOS switching transients. Regime I is however the key to the "non-conducting" mode ($V_{GS} = 0$), which can affect NFETs with short L in a quiescent off state. In any event, the regime I data are useful for extending the lower experimental energy limit of the observed $S_{it}(E)$, as will be seen later.

Data from only the first two regimes were considered in this section, to correspond to Eq. (23). We consider the quadratic regime first, due to the larger quantity of data available. The NFET data in this regime for all device types, various L, V_{GS}, and V_{DS} values (plotted as $y = (R_{ISG}/I_D{}^2)^{1/p}$ vs. $m_{EE}V_{EFF}$) are shown

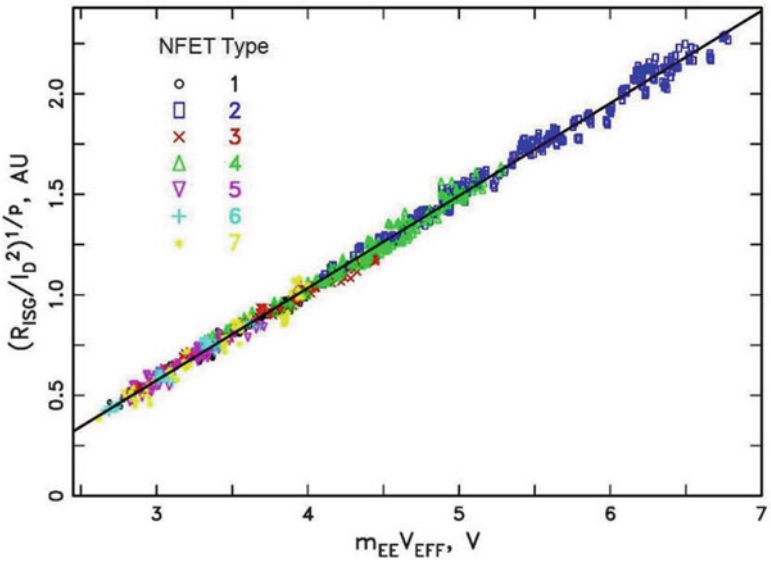

Fig. 10 Experimental data for all seven NFET device types in the quadratic regime

in Fig. 10. Nearly 1,000 device stresses are included in this figure. The values of $m_{EE} = 1.7 - 1.95$ (technology dependent) were suggested by simulation. The individual levels were adjusted for each device type to make the data "line up." The adjusted data follow the straight line fit displayed for $p = 13.5$. The x-intercept of this line is 1.75 V. Thus, these data imply that the $S_{it}(E)$ function can be expressed as,

$$S_{it} \propto (E - \phi_{it})^p, \tag{25}$$

with $\phi_{it} = 1.75 \pm 0.3$ eV, $p = 13.5 \pm 2$. These values are empirically based on the assumed form for S_{it}, and there is a tradeoff in the fit between ϕ_{it} and p. An ISG energy threshold of ~1.75 eV is consistent with the values reported by several authors for the minimum dissociation energy of Si–H bonds at the Si-SiO_2 interface [47, 48]. This form and these values are comparable to those from the literature, $\phi_{IT} = 1.6$ eV, $p = 14$ [1], and $\phi_{IT} = 1.5$ eV, $p = 11$ [3].

The "universal" nature of the energy driven model for NFETs in the quadratic (mid-V_G) regime is demonstrated by this plot down to a minimum dominant energy of ~2.6 eV ($V_{EFF} \sim 1.3$ V). This is important, since the mid-V_G regime, not regime III, typically dominates hot carrier degradation in a CMOS switching environment for lightly and moderately loaded circuits.

Next, NFET data in the linear regime are shown. The NFET data in this regime for all device types (plotted as $y = (R_{ISG}/I_D)^{1/p}$ vs. V_{EFF}) are shown in Fig. 11, again for $p = 13.5$. The data for $V_{EFF} > 2.5$ V follow the straight line with x-intercept of 1.75 V. However, below this potential, it deviates from this line, implying a low energy "tail" to the S_{it} function.

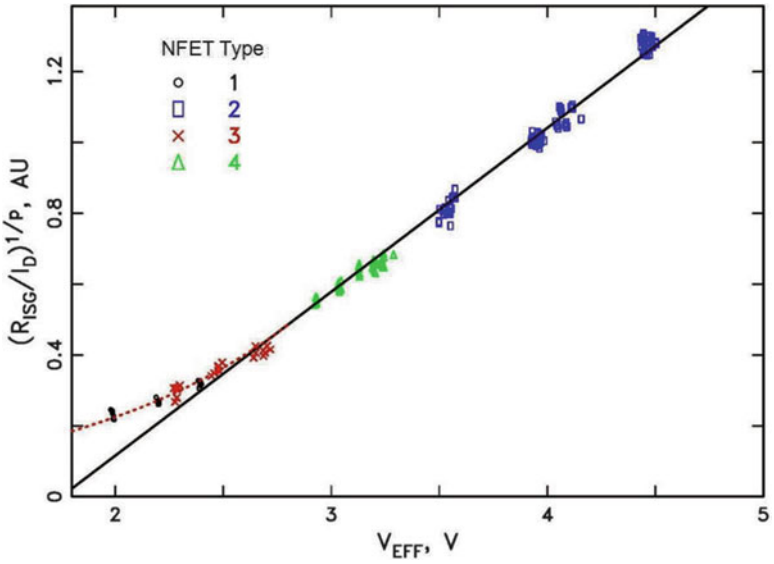

Fig. 11 Experimental data for four NFET device types in the linear regime

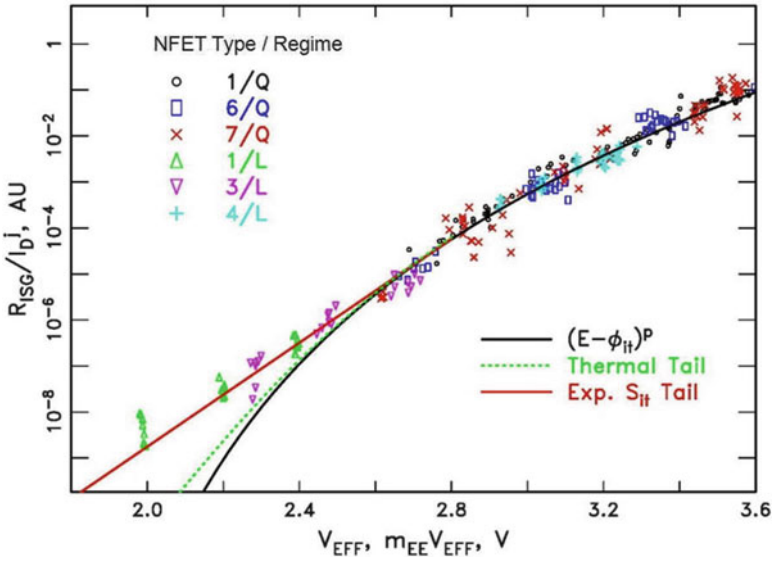

Fig. 12 Combined NFET Linear and Quadratic data at lower energies

The lower energy range is examined more closely in Fig. 12. Here, linear and quadratic data for dominant energies below 3.6 eV are combined (j = 1 for linear, 2 for quadratic regime), and now plotted on a logarithmic y-axis. The x-axis is V_{EFF} for the linear data, and $m_{EE}V_{EFF}$ for the quadratic data. The solid line is Eq. (25).

The calculated contribution from the thermal tail of the EEDF for the linear regime is the green dotted curve. This thermal contribution is much too small to explain the discrepancy. There are several possible mechanisms reported in the literature which could contribute to the observed tail: (1) an alternate weaker ISG pathway with a lower threshold energy [48–50], (2) bond energy dispersion due to SiO_2 disorder [50]. Since this tail is observed at low I_D, multiple vibrational excitation effects would not be expected to play a role [51, 52].

The red curve represents an approximation to the $S_{it}(E)$ function over the energy range down to about 2 eV, which can be fit to the following empirical form (adding an exponential tail to S_{it}):

$$\begin{aligned} S_{it} &\propto \exp(aE), \quad E \leq \phi_{it} + p/a \\ &\propto (E - \phi_{it})^p, \quad E > \phi_{it} + p/a \end{aligned} \tag{26}$$

with the following parameter values: $\phi_{it} = 1.75$ eV, $p = 13.5$, $a = 13\ eV^{-1}$.

7.2 PFET Hot Carrier Data

There are two major damage mechanisms in PMOSFETs that significantly compete with the ISG mechanism: (1) At low to medium overdrive, electron trapping causes V_T to decrease in magnitude, and I_{ON} (drive current) to increase. (2) At mid to high overdrive ($|V_{GS}|$ approaching or greater than $|V_{DS}|$), NBTI (enhanced by local self-heating) causes a decrease in $|V_T|$. ISG should be weaker in PFETs than in NFETs for two reasons-lower drain currents in PFETs, and lower available energy for holes (due to a higher critical field for velocity saturation, which leads to higher V_{DSAT}) [46, 53]. Due to these two competing mechanisms, it is difficult to unambiguously separate out ISG information from I–V measurements. From our database, we have taken data that we consider to be dominated by quadratic regime ISG, and plotted them in Fig. 13, (plotted as $y = (R_{ISG}/I_D{}^2)^{1/p}$ vs. $x = m_{EE}V_{EFF}$, $p = 13.5$). The straight line is consistent with the NFET energy driven hot carrier model parameters—x-intercept of 1.75 eV, and $p = 13.5$. There is evidence in the literature that a PFET energy driven hot carrier model does correlate with hot carrier measured in ring oscillators (at typical CMOS switching conditions) [46].

We have no unequivocal PFET ISG data in the linear regime. Because of competing electron trapping, our low V_G PFET hot carrier stresses contains increasing I_{ON} with time, or turnover (increasing, then decreasing I_{ON}), which results in high measured time slopes (>0.8), which are unphysical.

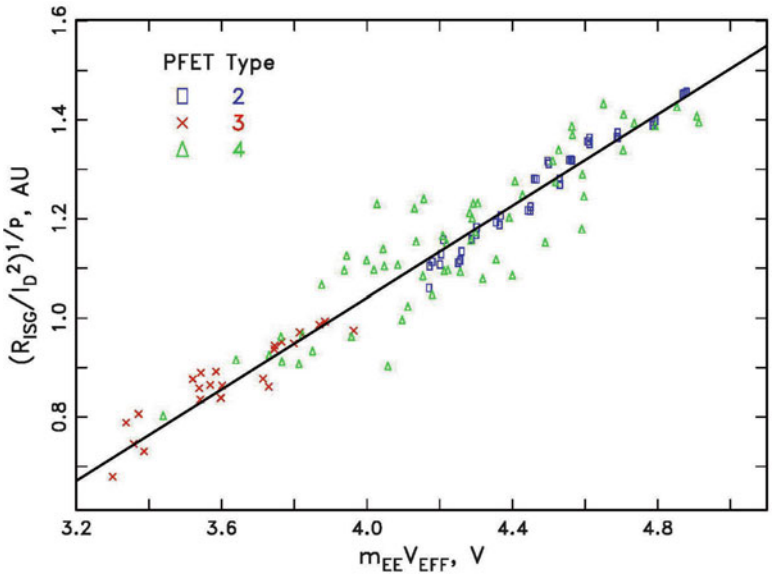

Fig. 13 Experimental data for three PFET device types in the quadratic regime (p = 13.5)

8 Justification of Energy Driven Model for ISG Damage Rates

There are three questions to be answered for ISG damage rates:

(1) Will the damage rate be energy driven in the quadratic regime?

Now that we have a provisional ISG scattering rate, Sit, we can revisit Sect. 4.2 for ISG. Recall the upper limit for an energy driven dominant energy:

$$qV_{EFF} \leq \frac{E_{TH}}{1 - p/\chi} \tag{27}$$

Now, for our experimental Sit function, $E_{TH} = 1.75$ eV, $p \sim 13.5$. This implies that a typical quarter micron device ($\chi_2 \sim 11$), or below, will be energy limited. For technologies of greater L_{nom} (say, $V_{DD} = 3.3$ V or more), ISG rates may be field driven at sufficiently high voltages.

(2) What are the conditions for the quadratic regime to dominate?

The relative impact of the carrier–carrier scattering tail to ISG can be roughly estimated in the following way. In Fig. 14, the ratio of $S_{it}(2V_{EFF})/S_{it}(V_{EFF})$ is plotted versus $V_{EFF.}$ Since the experimental measurements do not extend below ~2 V, that part of the curve is dashed. The energy driven model predicts that CCS driven hot carrier induced ISG becomes stronger with supply voltage scaling down to $V_{EFF} \sim 1.8$ V. Of course, device dimension scaling will also

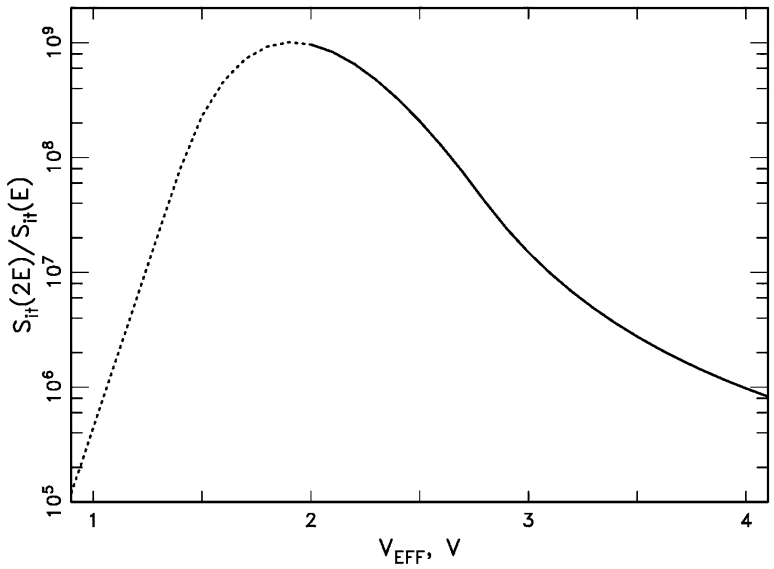

Fig. 14 Ratio of Experimental ISG rate at CCS knee to that at base knee. Dashed section is extrapolated below data

increase CCS due to an increase in carrier concentration. However, beginning below ~1.7 V, CCS effects may become significantly weaker. Although this is speculative, a potential danger exists that extrapolating measured quadratic regime (mid-V_G) stress data to use conditions below $V_{EFF} = 1$ V ($V_{DD} \sim 0.8$ V or so) may seriously underestimate the field exposure to hot carrier, which will be dominated by the linear regime.

(3) How good is the approximation (Eq. (23)) for the quadratic regime?

According to Eq. (23), if the CCS tail dominates the hot carrier damage,

$$\frac{R_{ISG}\,(V_{EFF})}{{I_D}^2} = \int f(E) S_{it}(E) dE \approx A_2 S_{it}\,(qm_{EE} V_{EFF}) \tag{28}$$

The numerical integral evaluated for the idealized EDF CCS tail, f_{I2}, is compared against $S_{it}(2qV_{EFF})$ in Fig. 15. The agreement is very reasonable. There are partially compensating errors due to approximating the integral using only the peak integrand, and neglecting the weak V_{EFF} dependence of f_{I2} in Eq. (23). Given the simplified and idealized (and somewhat empirical) nature of the energy driven model as presented here, the experimental $S_{it}(E)$ function will differ somewhat from any "actual" cross section.

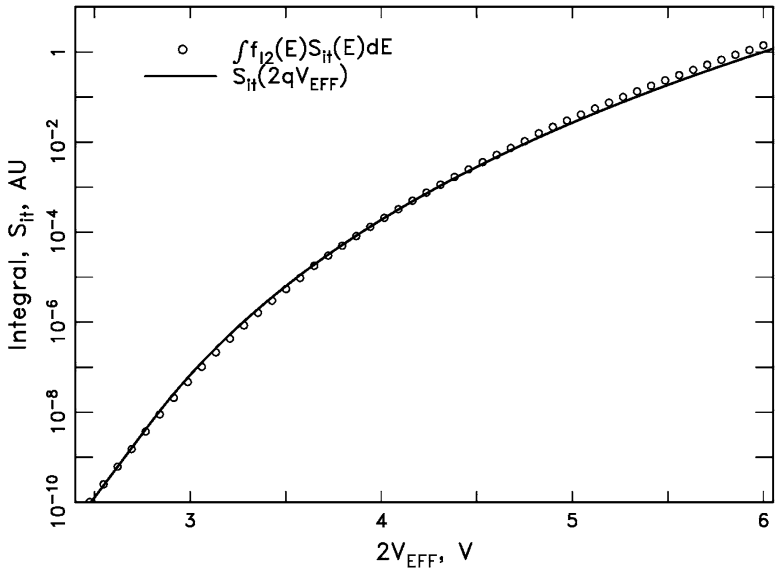

Fig. 15 Comparison of R_{ISG} integral with S_{it}

9 Temperature Dependence

The energy driven model can be extended to cover temperature dependence by introducing the correct temperature dependencies of all its parameters. Traditionally, the major temperature effect to hot carrier was attributed to the change of λ, the mean free path with temperature. The generally accepted expression was introduced by Crowell and Sze in 1966 [54]:

$$\lambda(T) = \lambda_0 \tanh\left(E_R/2kT\right), \tag{29}$$

where $E_R = 63$ meV is the optical phonon energy in silicon. Around room temperature λ is a rather weakly decreasing function of temperature; its value at $T = 400$ K is 0.86 of its value at 300 K. However, in the lucky electron model, it appears in an exponential, so that the net effect is sharply reducing hot carrier rates with increasing temperature. This effect is embodied in the energy driven model by the parameter χ of the base distribution (or χ_1), which is conceptually $\propto 1/\lambda$. By Eqs. (16), (20a), and (21), the impact ionization rate, and the ISG rates in both the linear and quadratic regimes will all have the same χ_1 dependence, $e^{-\chi_1}$. Assuming $\chi_1 \propto 1/\lambda$, and using Eq. (29), the net temperature dependence of this term from 200 to 400 K can be approximated by T^{-nt}, where $nt \approx 0.4\chi_1$ (300 K). Thus, with scaling, the effect of mean free path temperature dependence declines, becoming very small at or below an $L_{nom} = 50$ nm technology, and probably disappears entirely as the

nominal channel length drops down to 25 nm or below. Other parameters will drive the overall hot carrier rate temperature dependence.

First we consider impact ionization. The temperature dependence of Eq. (16) is,

$$r_{ii}(T) \approx A'(T)e^{-\chi(T)}[qV_{EFF}(T) - E_G(T)]^{4.6} \tag{30}$$

We write A′(T) because the integration in Eq. (16) introduces a positive temperature dependence of T^{0-1}. (The effective width of the integrand increases with T.) We have already discussed the χ dependence. These two competing terms are combined together into an empirical temperature dependent prefactor,

$$A'(T)e^{-\chi(T)} \approx A''T^{-nt} \tag{31}$$

For E_G(T), we use Sze [55]:

$$E_G(T) = 1.17eV - \frac{0.000473\ eV/K \cdot T^2}{636 + T} \tag{32}$$

Expanding V_{EFF}(T),

$$V_{EFF}(T) = V_0(T) + V_{DS} - V_{DSAT}(T) \tag{33}$$

The V_{DSAT}(T) dependence is mostly due to that of F_C and V_T. (The small temperature dependence of m is ignored.)

$$F_C(T) = \frac{v_{sat}(T)}{\mu_{eff}(T)} \tag{34}$$

which we will take as approximately ∝T for NFETs. V_T is determined directly from measurements on stresses devices. V_0(T) would be expected to be ∝T, however, we take the empirical approach. As an example, in Fig. 16, $r_{ii}^{1/4.6}$ is plotted vs. $V_{DS} - V_{DSAT} - E_G/q$ for Device 1, NFET, L = 65 nm, and T = 233, 303, 398 K. Empirical V_0 values from these fits are 0.220, 0.285, and 0.377 V for T = 233, 303, 398 K. In this case V_0 is very nearly proportional to T, and the slope is unchanged with temperature, however this is not true for all devices measured. (nt = 0) The model developed to fit experimental data is,

$$V_0(T) = V_0\,(L,\ \ T = 300K) + TC_V \cdot (T - 300) \tag{35}$$

Using this model, the impact ionization data at low overdrive for a particular device type at various temperatures and channel lengths can be made to fit on one curve. Figure 17 shows temperature data for device types 1 and 2, chosen as examples of scaling effects.

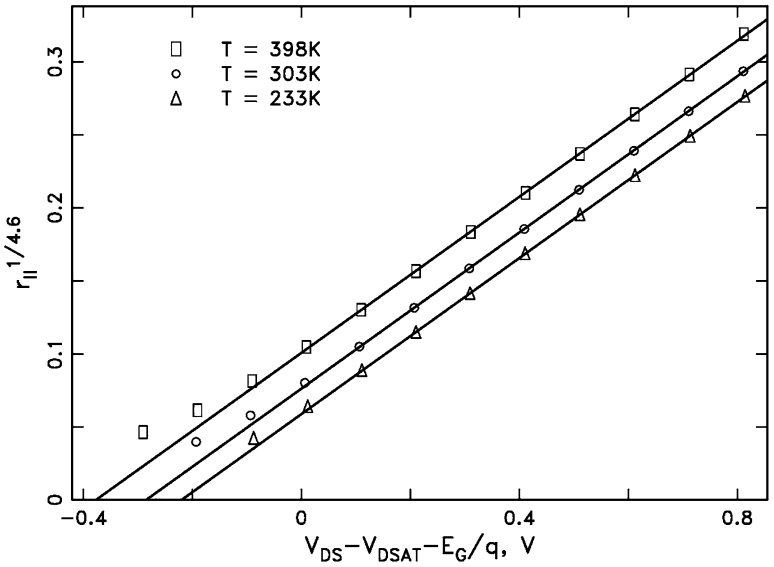

Fig. 16 *Points*: Measured impact ionization ratio, $r_{ii}^{1/4.6}$, for L = 65 nm, and three ambient temperatures, T, of device type 1, NFET versus calculated $V_{DS} - V_{DSAT}(T) - E_G(T)/q$. *Lines*: straight line fits

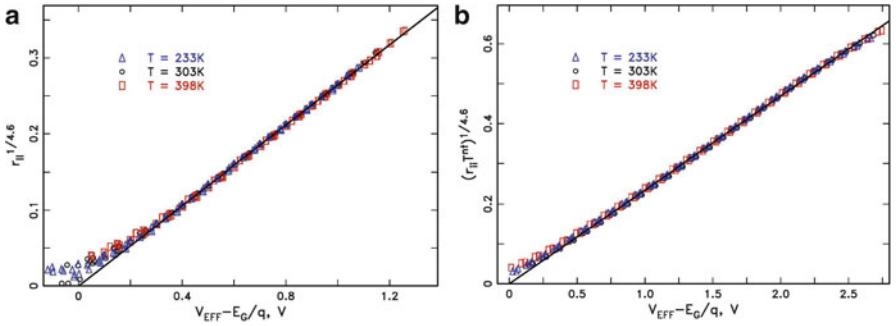

Fig. 17 Measured impact ionization ratio, $r_{ii}^{1/4.6}$, for various channel lengths, L, and three ambient temperatures, T, of device type 1 and 2, NFET versus calculated $V_{EFF} - E_G(T)/q$. *Lines*: straight line fits through the origin. (**a**) Type 1, NFET, L = 45–120 nm ($TC_V = 0.0010$) (**b**) Type 2, NFET, L = 0.18–0.24 μm ($TC_V = 0.0009$, nt = 0.5)

The hot carrier induced current shifts at a typical mid Vg stress bias condition, but three temperatures, for these same device types are shown in Fig. 18, along with the model predictions with the same parameters as for the impact ionization.

The observed temperature dependence is well matched by the model. Note that there are opposite temperature dependencies for these two device types—whereas the quarter micron NFET displays the classic behavior of negative temperature

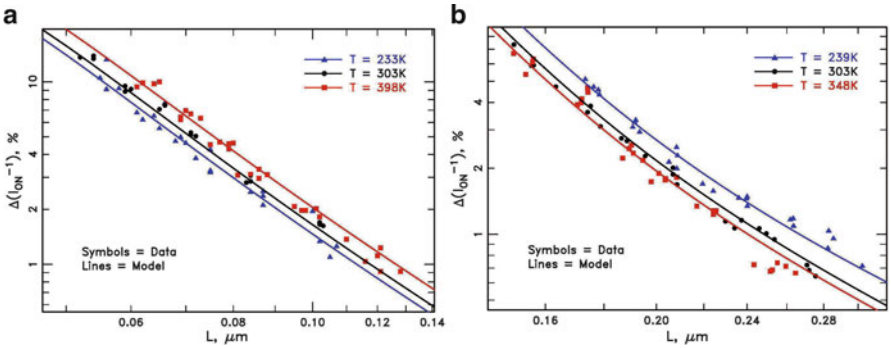

Fig. 18 Hot carrier induced current shift, $\Delta(I_{ON}{}^{-1})$,%, versus channel length, L, for three ambient temperatures, T, of device type 1 and 2, NFET. Lines: model predictions. (**a**) Type 1, NFET, t = 3,000 s, Stress: $V_{DS} = 1.9$ V, $V_{GS} = 1.0$ V (**b**) Type 2, NFET, t = 1,000 s, Stress: $V_{DS} = 3.3$ V, $V_{GS} = 1.65$ V

Table 5 Temperature effects of model parameters (ratio of shift at 125°C to that at −40°C)

Parameter	1, NFET	2, NFET
V_T	0.91	0.96
μ	0.72	0.65
F_C	0.74	0.73
V_0	2.85	1.83
Prefactor	1.00	0.77
Overall net ratio	1.40	0.64

coefficient, the hot carrier shift of the 63 nm NFET increases with temperature. We explore this further by calculating the effect on shift given by the temperature dependencies of these five parameters—V_T, μ, F_C, V_0 and prefactor. Table 5 gives the modelled ratio of $\Delta(I_{ON}{}^{-1})$ at 398 K (125°C) to that at 233 K (−40°C) induced by each of these parameters alone (all others fixed at their 30°C values) at $L = L_{nom}$.

The scaling effects are mainly due to only two of these parameters—V_0 and prefactor. As technology scales down, the reduction in supply voltage and the possible increase in V_0 (due to stronger halos) significantly increase the positive impact of a modest available energy increase with temperature. Also, as channel length decreases, the negative temperature effect of mean free path (as reflected by the prefactor) diminishes.

10 Summary and Discussion

The energy driven model is demonstrated for the impact ionization process in NFETs and PFETs by experimental measurements in $V_{DD} = 1.2$ and 2.5 V class devices. NFET impact ionization follows the generally accepted energy dependence

($p = 4.6$), and energy threshold ($E_{TH} = E_G$) quite well. The experimentally parameters for PFET impact ionization are $p \sim 7$, and $E_{TH} = E_G$. These parameters are unclear in the present literature.

The energy driven model has been quite successful in empirically fitting experimental NFET hot carrier degradation data over a wide range of technology nodes. As demonstrated in Figs. 10, 11, and 12, this model allows for a nearly universal description of hot carrier behavior for NFET devices from the quarter-micron down to the 14 nm technology node. PFET hot carrier degradation results are consistent with this model, as well. There is no adjustment of voltage dependence slope or acceleration function necessary between technology nodes (as in the Lucky Electron Model), since this is essentially fixed by the S_{it} function. The major parameters to be determined experimentally for each node are simply the levels [A_1 and A_2 in Eq. (23)]. When the model parameters are properly adjusted for temperature, the net temperature dependence of hot carrier degradation is also predicted correctly.

The experimental S_{it} function is extremely 'soft'—that is, it has no sharp 'knee' points. Of course, the observed energy dependence is "smeared out" by the energy width of the $f(E)S_{it}(E)$ product, spatial variation of f(E), and possible partial occupancy of multiple vibrational states higher than the ground state, which would lower the energy needed for a solitary large energy interaction to generate an interface state [51]. The data above 2.5 eV do suggest an energy threshold of ~1.75 eV. However, below 2.5 eV, S_{it} is higher than expected from a single energy threshold model. Possible explanations for this deviation are: (1) H bond energy dispersion due to SiO_2 disorder [51]. (2) Multiple pathways to H desorption [48–50]. However, no structure is seen that would relate to a second, lower, energy threshold. Extending the data to lower energies may elucidate this question. These effects would result in a very complex, and perhaps 'soft' cross section, due to the complexity of the defect creation. In this picture, the S_{IT} function proposed here must be considered an *effective* ISG cross section for hydrogen desorption.

References

1. S. Rauch, G. La Rosa, IEEE Trans. Device Mater. Reliab., **5**, 701 (2005)
2. C. Hu et al., IEEE Trans. Electron Devices **32**, 375 (1985)
3. C. Guérin, IEEE Trans. Device Mater. Reliab. **7**, 225 (2007)
4. W. Shockley, SSE **2**, 65 (1961)
5. J. Townsend, *The Theory of Ionization of Gases by Collision* (Constable, London, 1910)
6. G. Baraff, Phys. Rev. **128**, 2507 (1962)
7. B. Ridley, J. Phys. C: Solid State Phys. **16**, 3373 (1983)
8. N. Goldsman et al., JAP **68**, 1075 (1990)
9. A. Pacelli et al., J. Appl. Phys. **83**, 4760 (1998)
10. O. Rubel et al., Phys. Status Solid C **1**, 1186 (2004)
11. S. Kasap et al., J. Appl. Phys. **96**, 2037 (2004)
12. N. Goldsman et al., IEEE Electron Device Lett. **11**, 472 (1990)
13. P. Ko, et al., in *IEEE IEDM Tech. Dig.* (1981), p. 600

14. Y. Taur, T. Ning, *Fundamentals of Modern VLSI Devices* (Cambridge University Press, Cambridge, 1998), pp. 156ff
15. J. Jakumeit, U. Ravaioli, Physica B **314**, 363 (2002)
16. M. Chang et al., in *Proceedings of ESSDERC* (1996), pp. 263
17. J. Bude, M. Mastrapasqua, IEEE Electron Device Lett. **16**, 439 (1995)
18. F. Venturi et al., IEEE Trans. Electron Devices **38**, 1895 (1991)
19. P. Childs, D. Dyke, SSE **48**, 765 (2004)
20. P. Scrobahaci, IEEE Trans. Electron Devices **41**, 1197 (1994)
21. A. Ghetti et al., IEEE Trans. Electron Devices **46**, 696 (1999)
22. N. Sano, M. Tomizawa, IEEE Trans. Electron Devices **42**, 2211 (1995)
23. T. Mietzner et al., IEEE Trans. Electron Devices **48**, 2323 (2001)
24. L. Keldysh, Soviet Phys. JETP **10**, 509 (1960)
25. Y. Kamakura et al., J. Appl. Phys. **75**, 3500 (1994)
26. P. Childs, D. Dyke, Solid State Electron **48**, 765 (2004)
27. S. Huang et al., in *IEEE IEDM Technical Digest* (2001), p. 237
28. S. Zanchetta et al., Solid State Electron **46**, 429 (2002)
29. Y. Pang, J. Brews, IEEE Trans. Electron Devices **49**, 2209 (2002)
30. Y. Taur, T. Ning, op. cit., pp. 150, 151
31. T. Kunikiyo et al., J. Appl. Phys. **79**, 7718 (1996)
32. P. Childs, C. Leung, Electron. Lett. **31**, 139 (1995)
33. P. Childs, C. Leung, J. Appl. Phys. **79**, 222 (1996)
34. M. Chang et al., J. Appl. Phys. **82**, 2974 (1997)
35. D. Ventura et al., Numer. Funct. Anal. Optim. **16**, 565 (1995)
36. M. Fischetti, S. Laux, in *IEEE IEDM Technical Digest* (1995), p. 305
37. S. Rauch et al., IEEE Electron Device Lett. **19**, 463 (1998)
38. S. Rauch et al., IEEE Trans. Device Mater. Reliab. **1**, 113 (2001)
39. L. Su et al., in *IEEE Symposium on VLSI Technology Digest* (1996), p. 12
40. V. Chan et al., in *IEEE IEDM Technical Digest* (2003), p. 77
41. F. Arnaud et al., in *IEEE IEDM Technical Digest* (2009), p. 651
42. A. Paul et al., in *IEEE IEDM Technical Digest* (2013), p. 361
43. R. Woltjer, G. Paulzen, in *IEEE IEDM Technical Digest* (1992), p. 535
44. R. McMahon et al., in *Technical Proceedings of 2002 International Conference on Modeling and Simulation of Microsystems* (2002), p. 576
45. 6_Bravaix
46. S. Rauch et al., IEEE Trans. Device Mater. Reliab. **10**, 40 (2010)
47. S. Pantelides et al., IEEE Trans. Nucl. Sci. **47**, 2262 (2000)
48. B. Tuttle et al., Phys. Rev. B **59**, 12884 (1999)
49. K. Hess et al., Appl. Phys. Lett. **75**, 3147 (1999)
50. C. Van de Walle, B. Tuttle, IEEE Trans. Electron Devices **47**, 1779 (2000)
51. B. Tuttle, W. McMahon, K. Hess, Superlattice Microstruct. **27**(2/3), 229–233 (2000)
52. K. Hess et al., Physica B **272**, 527–531 (1999)
53. S. Rauch, G. La Rosa, in *IEEE IRPS, Tutorial #124* (2010)
54. C. Crowell, S. Sze, Appl. Phys. Lett. **9**, 242 (1966)
55. S. Sze, *Physics of Semiconductor Devices* (Wiley, New York, 1981), p. 16

http://www.springer.com/978-3-319-08993-5

Hot Carrier Degradation in Semiconductor Devices

Grasser, T. (Ed.)

2015, X, 517 p. 352 illus., 253 illus. in color., Hardcover
ISBN: 978-3-319-08993-5